Sensors & Actuators: B. Chemical 410 (2024) 135628

Contents lists available at ScienceDirect

Sensors and Actuators: B. Chemical

journal homepage: www.elsevier.com/locate/snb

Terahertz Lattice enhanced Quasi-Anapole Immunosensor assisted by protein antibody and AuNPs

Chengcheng Luo [a], Thomas Tan CaiWei [b], Zhiyuan Fan [a], Lin Chen [a,c,*], Ranjan Singh [b,**], Yiming Zhu [a,*], Songlin Zhuang [a]

[a] Technology Cooperative Innovation Center, Shanghai Key Lab of Modern Optical System, University of Shanghai for Science and Technology, Shanghai 200093, China
[b] Centre for Disruptive Photonic Technologies, Division of Physics and Applied Physics, School of Physical and Mathematical Sciences, Nanyang Technological University, Singapore 637371, Singapore
[c] Shanghai Institute of Intelligent Science and Technology, Tongji University, Shanghai 200092, China

ARTICLE INFO

Keywords:
Immunosensor
Quasi-Anapole
Lattice
Limit of detection
Spike protein

ABSTRACT

Terahertz (THz) metasurface immunosensor has the characteristics of label-free detection, good biocompatibility and high specificity because the antibody-modified of biomarkers has the ability to specifically recognize corresponding biomarkers and increase the detection sensitivity to the concentration of the recognized antigen. The limit of detection (*LoD*) of THz metasurface immunosensor is highly dependent on resonant field enhancement of metasurface. The anapole mode shows a radiationless state with nontrivial oscillating current configuration. To observe such mode in farfield, in this work, the concept of quasi-anapole (QA) mode is presented which is induced when the electric and toroidal dipoles with identical intensity radiate in antiphase on the metasurface with the unit cell of two split ring resonators (SRRs) on both sides of the central cut-wire. In addition, by coupling the first-order lattice mode to the QA mode, lattice-enhanced QA mode (LQA) was investigated and observed to further enhance field confinement and decrease radiative loss. As a practical application, immunosensor was designed and fabricated by functionalized gold nanoparticles conjugated with the specific monoclonal antibody onto the LQA metasurface to detect the cell concentration of SARS-CoV-2 spike protein. The experimental results indicate that the response of LQA immunosensor depends heavily on the concentration of the Anti-S modified on its surface. When the concentration of Anti-S is 50 pg/ml, the *LoD* reaches to 3 pg/ml (39 fmol). Such THz LQA immunosensor also shows good specific identification and validates its effectiveness in biomedical sensing.

1. Introduction

The terahertz (THz) region of the electromagnetic spectrum referred to technological gap between the infrared and microwave frequencies. The low photon energy of THz wave, about 4.1–40 meV, made it almost impossible to produce harmful ionization to destroy biological tissue [1–5]. Likewise, due to the good penetrability of THz waves [6,7], it is easy to penetrate nonpolar materials. Therefore, THz technology is suitable for biomedical detection [8], imaging [9] and sensing [10]. However, a commonly employed method for conducting spectroscopic measurements on samples within the THz frequency range involves the amalgamation of the powdered sample with a binding medium. This resulting mixture is subsequently compressed into a pellet and positioned in the trajectory of the radiation. While this technique is straightforward and firmly established, it proves unsuitable when dealing with exceedingly minute sample quantities and trace sensing applications.

The metasurface is a 2D forms of metamaterials that is often made up of an array of unit elements with a subwavelength thickness [4,11–13]. Moreover, it has extraordinary physical properties which are not found in natural materials [14–16]. Metasurface has preeminent capabilities to confine electromagnetic fields and enhance the interactions between light and matter, providing high sensitivity to changes of the environment. They regard as the potential sensing platforms as they could be easily fabricated on different types of substrates [17–19]. THz metasensor platforms have been widely used in biomolecular detection for

* Corresponding author at: Technology Cooperative Innovation Center, Shanghai Key Lab of Modern Optical System, University of Shanghai for Science and Technology, Shanghai 200093, China.
** Corresponding author.
E-mail addresses: linchen@usst.edu.cn (L. Chen), ranjans@ntu.edu.sg (R. Singh), ymzhu@usst.edu.cn (Y. Zhu).

https://doi.org/10.1016/j.snb.2024.135628
Received 18 January 2024; Received in revised form 4 March 2024; Accepted 8 March 2024
Available online 9 March 2024

decades due to their low cost, high sensitivity, rapid response, and label-free detection [20,21]. Some different enhanced modes have been developed for achieving good sensing performances [22,23]. For instance, I-shape metasensor design was proposed to enhance sensitivity by optimizing the value of the mode volume of the metamaterial resonantly confined fields [24]. In addition, dual torus toroidal mode was excited in overlapped split ring resonators (SRRs) metasensor which is capable of detecting the ethanol-water mixture solution with high sensitivity [25]. Soon after, quasi bound state in the continuum mode (QBIC) was also excited and illustrated to achieve metasensor with high sensitivity by coating Ge film [26]. Moreover, a topological sensor consists of a topological waveguide critically coupled with high *Q* topological cavity was demonstrated with sensing performance figure of merit (*FOM*) up to 4000 RIU/mm^{-1} [27]. Particularly, immunosensor is a kind of biosensor that shows high specificity because the antibody-modified of biomarkers has the ability to specifically recognize corresponding biomarkers and increase the sensitivity to the concentration of the recognized antigen. For example, inductive-capacitive (LC) resonant mode of immunosensor combined with CA125 antigen antibody binding technology can specifically identification cancer biomarkers with the *LoD* of 0.01 U/ml [28]. The toroidal metasurface with high quality (*Q*) factor is also a reliable platform for immunosensing applications. Such immunosensor was utilized to detect Zika-viru envelope protein using a specific Zika-virus antibody with the *LoD* of 24.2 pg/ml [29]. Although current THz immunosensor are promising, the performance of *LoD* can be further improved by designing suitable immunosensor with higher *Q*-factor and *FOM*.

The anapole mode, which arises as a result of the destructive interference between electric dipole (ED) and toroidal dipole (TD) moments with the same intensity and opposite phase [30], gained much attention to the researchers in the microwave [31], THz [32–35], and optics [36–39] frequency ranges. Compared with other modes such as LC, Fano, and toroidal modes, anapole modes has better sensing performance due to the significant enhancement in the confined field and the dramatic narrowing in the linewidth realized by the effective coupling of ED and TD. However, since anapole mode is a nonradiative resonance, it appears to be invisible in the far-field [40], which hinders many applications. In this work, the concept of "Quasi-Anapole" (QA) is presented and excited, which can be transformed from the nonradiative anapole mode when EDs and TDs have same radiation intensity and observed in far-field. In addition, the lattice mode arises from the collective Rayleigh scattering of periodic structures, where energy is strongly concentrated on the surface that fails to radiate to the far-field. So they are known as diffractive modes or Wood's anomalies, manifest as discontinuities in the transmission/reflection spectra of metamaterials [41,42]. The resonance frequency of lattice mode can be tuned by altering the periodic of meta-atoms [43]. Currently, the interactions between lattice and LC [44], Fano [45], and QBIC [46] modes have been reported, and the results of these studies have been applied to the field of highly sensitive sensing [23].

To our knowledge, the lattice regulation of QA has not been reported. Here, the lattice mode is introduced to couple with QA mode to further enhance *Q*-factor by changing the lattice period of the structure. As the typical application, we also reported the results of spike (S) protein detection by using Lattice enhanced QA (LQA) modes of THz immunosensor. Fig. 1(a) shows the proposed immunosensor under the illumination of THz waves. The unit cell of the immunosensor consists of a pair of mirrored metallic SRRs and a cut-wire between them, fabricating on a 500 μm-thick high-resistivity (5 kΩ·cm^{-1}) silicon substrate (n = 3.42) with the size of 1 cm × 1 cm. All metallic patterns are fabricated by projection step photolithography followed by the deposition of 10 nm Cr and 150 nm Au layers with conductivity of 4.56 × 10^7 S/m by magnetron sputtering. Both *Q*-factor and *FOM* were improved by coupling the QA mode and the lattice mode that is inherent in metamaterial periodic arrays (the top of Fig. 1(c)). Under *y*-polarized plane wave illumination, circulating currents (blue arrows) in left and right loops of SRRs and the ED moment (violet arrow) in metal wire resonator can be induced. Due to the circulating currents of the dual SRRs in the opposite direction, an out of plane circulating magnetic field (red arrow) can be induced and subsequently excite the *y*-directed TD (green arrow) in the position of the ED. When TD and ED possess the identical intensity as well as out of phase, the destructive interference between them leads to the QA mode, accompanied by the strong field confinement, as depicted in the bottom of Fig. 1(c). We also investigated the mutual coupling between the lattice mode and the QA resonance, whereby the QA resonance shows ultrahigh *Q*-factor of up to 89. We used such LQA immunosensors for rapid detection of S proteins, as displayed in Fig. 1(b). Current biological-based methods suffer from time consuming for polymerase chain reaction tests [47] or low accuracy and sensitivity for lateral flow immunoassay [48,49]. In our proposed THz immunosensor platform, the sensitivity and *LoD* were improved after modifying the immunosensor with gold nanoparticles (AuNPs) and antibodies. By varying the concentration of the antibody, experimental results revealed a different regular pattern of antigen concentration and frequency drift of the immunosensor. The optimal *LoD* was found for the concentration of 50 pg/ml antibody. In experiments, *LoD* can achieve as low as 3 pg/ml

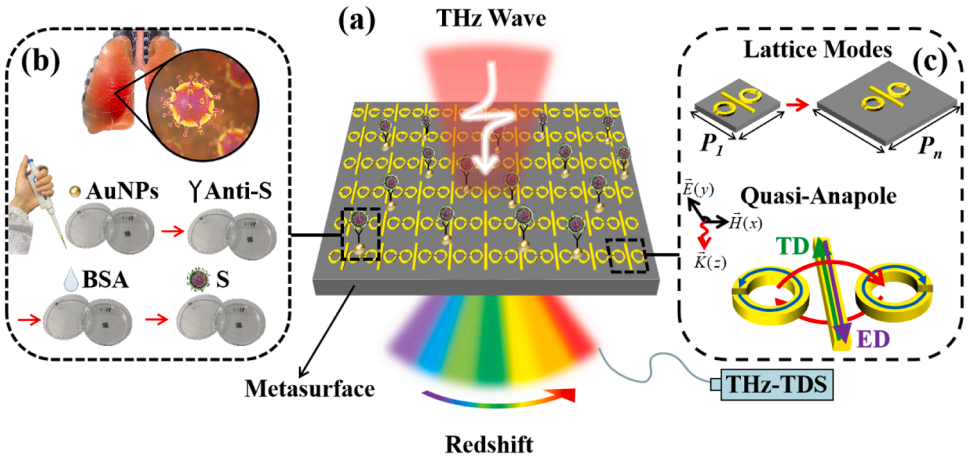

Fig. 1. The schematic of the sensing strategy based on the proposed LQA immunosensor. (a) The transmission dip variations are captured by the terahertz time domain spectroscopy (THz-TDS) when THz waves illuminating on the metasurface. (b) S protein with increasing concentrations are cultured on the immunosensor in an environment conducive to cell reproduction. (c) The period-agile unit cell consists of the cut-wire and SRRs for governing lattice mode and QA mode, respectively; (bottom) schematic of the excitation of toroidal dipole (TD) and electric dipole (ED) in the unit cell; blue arrows: circulating surface currents in left and right loops of SRRs; red arrows: the head-to-tail magnetic moment.

(39 fmol). To further evaluate the specificity of detection, four proteins (Aβ40 , Aβ42 , CEA and S protein) were utilized to explore the specific response of the LQA immunosensor. Experimental results show that the modified sensor is only sensitive to S protein rather than other proteins. The proposed LQA metasurface exhibits ultrahigh *Q*-factor and excellent *LoD*, which lays the foundation for the application of highly sensitive and specific protein detection.

2. Simulation and discussion

2.1. The pattern of a cut-wire located between the SRRs with gaps towards wire (pattern I)

We first analyzed symmetric plasmonic unit cell which is composed of a cut-wire located between the SRRs with gaps towards wire. Full-wave simulations by using a commercially available frequency-domain solver Computer Simulation Technology Microwave Studio were performed to explore the influence of period on the transmission spectra

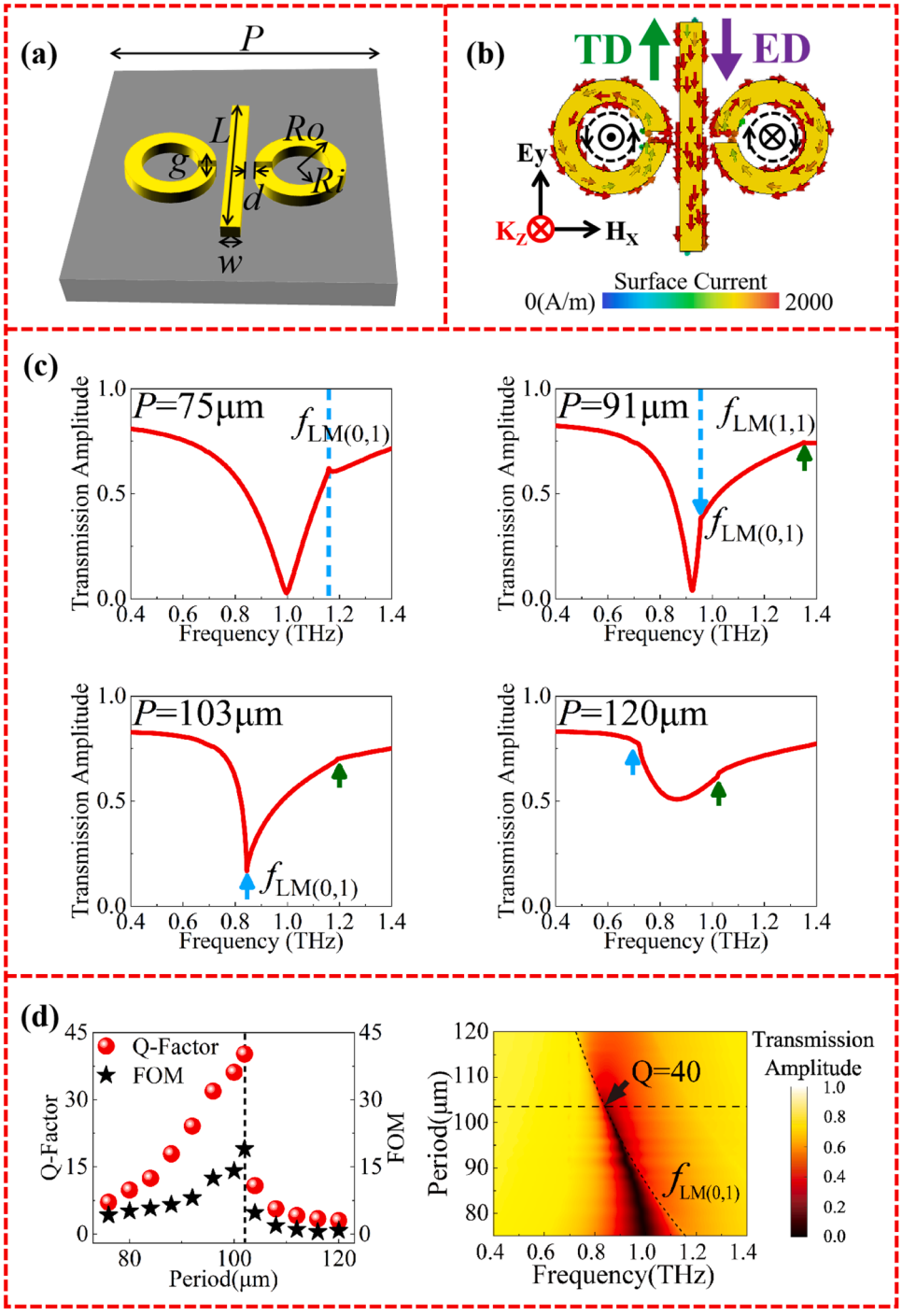

Fig. 2. (a) Unit cell of the metasurface, whose structural parameters are $P = 96$ μm, $Ro = 15$ μm, $Ri = 9$ μm, $d = 3$ μm, $w = 6$ μm, $L = 60$ μm. (b) The simulated surface currents at the resonance dip with the period of 103 μm (0.842 THz). (c) Coupling resonances of QA and lattice modes. Simulated transmission amplitude of metamaterials with lattice periods from $P = 75$–103 μm. (d) Left: *Q*-factor and *FOM* of the QA resonance at different lattice periods of the metamaterials. Right: The 2D map of transmission amplitude as a function of the period and frequency of the incident THz wave.

and simulated surface currents at resonance dip. Fig. 2(a) and (b) show the unit cell with the geometrical dimensions and simulated surface currents at the resonance dip with the period of 103 μm (0.842 THz). The physical origin of this resonance can also be found in Fig. 2(b). There is a pair of counter-rotating surface currents along the two SRRs, which is excited by the ED in cut-wire along *y*-direction. Each can generate a magnetic component with head to tail and induce TD. Interestingly, the excited TD and ED are out of phase and show destructive interference with different intensity, which can be regarded as QA mode.

Then we discussed the interaction between lattice mode and QA mode. Lattice mode coupling is accomplished by tuning the frequency of the lattice mode, denoted as f_{LM}.

$$f_{LM} = \frac{c}{nP}\sqrt{i^2 + j^2}, \tag{1}$$

where c is the speed of light in vacuum, n is the refractive index of the substrate, P is the lattice period, and (i, j) are non-negative integers defining the order of the lattice mode. Eq. (1) implies that the frequency of lattice mode is directly associated with the refractive index of the substrate. In the simulation, the periodicity (P) of the structure is varied from 75 μm to 120 μm, as shown in Fig. 2(c). By increasing the period from 75 μm to 120 μm, the spectral position of the lattice mode shows redshifts according to Eq. (1), in order to overlap the QA mode. Through this coupling, the QA resonance also redshifts, and their spectral line-width changes. For the lattice period of 75 μm, the lattice mode (cyan dotted line) is located at 0.998 THz. As the lattice period is increased from 75–103 μm, resonance coupling between QA mode and lattice mode is observed, which significantly decreases the resonance intensity and narrows the line-width. The *Q*-factor can be calculated as $f_0/\Delta\nu$, where $\Delta\nu$ is the full width at half maximum (FWHM) of the resonance and f_0 is the resonance frequency, and the *FOM* can be defined as $FOM = Q \times I$ [50], where I is the resonant transmission change in terms of intensity. To systematically study the optimized structure and the coupling effects, the *Q*-factor and the *FOM* of the LQA with respect to the lattice period is plotted in Fig. 2(d) as P is swept from 75 μm to 120 μm. The *Q*-factor increases gradually from 11.9 to 38 (see Fig. 2(d), left). This increase is due to the modulation of the lattice mode to the QA that confines the electromagnetic energy in the metamaterial array. As the lattice resonance frequency is lower than the QA resonance frequency, the QA resonance broadens. The *FOM* of the QA also reaches a maximum of 19 at $P = 103$ μm. Lattice resonance frequency variation with respect to the lattice period is also plotted (green dashed-dotted line) (see Fig. 2 (d), right). It clearly depicts a redshift of the QA and lattice resonance

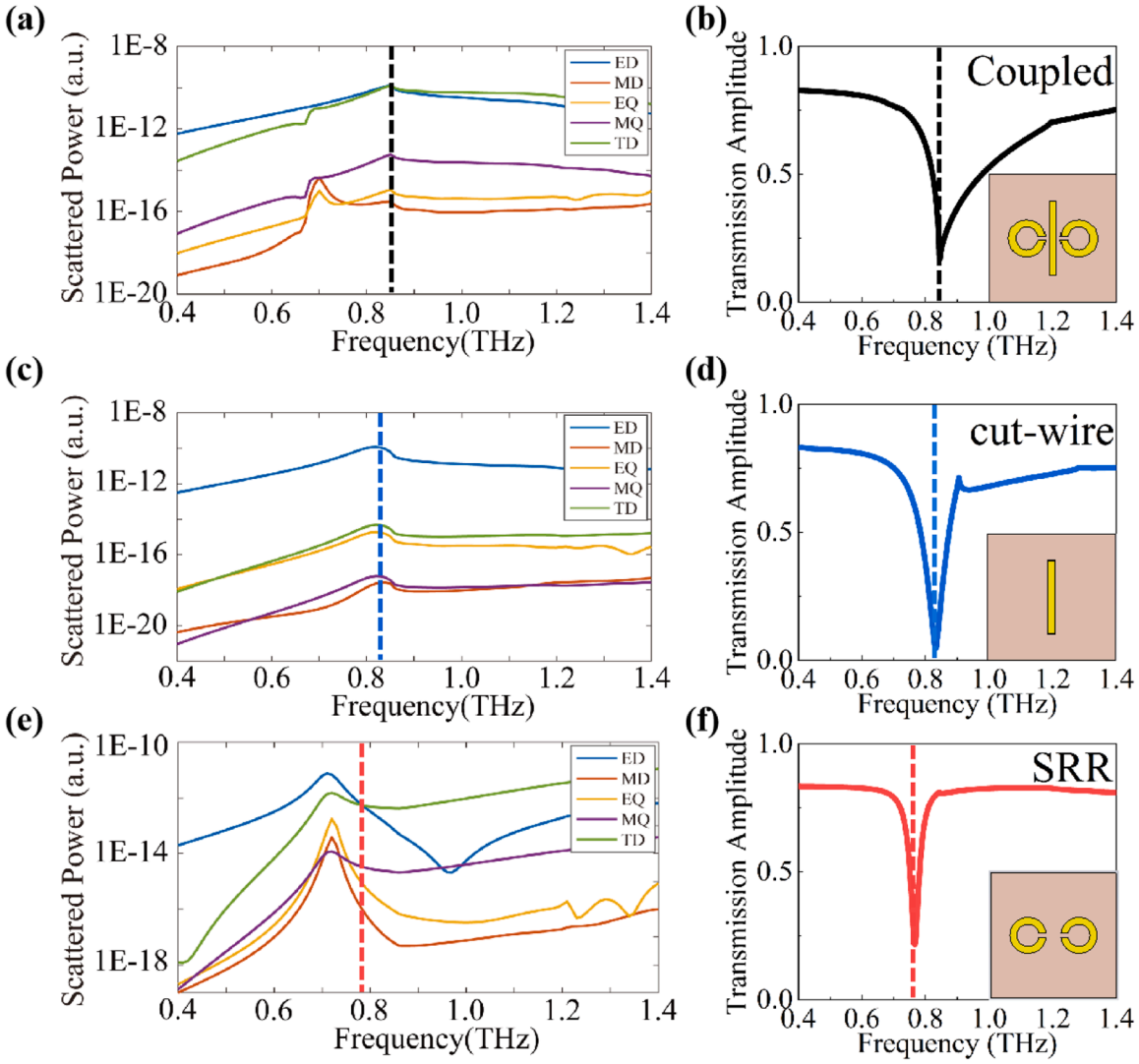

Fig. 3. Multipole far-field scattering of (a)(b)coupled structure (c)(d) individual cut-wire (e)(f) two split ring resonators. Five leading scattered powers of multipole decomposition for the planar metamaterial, where ED, MD, EQ, MQ, and TD are electric dipole, magnetic dipole, toroidal dipole, electric quadrupole, and magnetic quadrupole, respectively.

frequencies. As lattice resonance frequencies approaches and matches the QA resonance, the coupling leads to narrowing of the resonance line-width due to the increased diffraction effects that traps the energy in the metamaterial array and suppresses the far-field radiation energy near the resonance.

Multipole decomposition can enable an accurate calculation of the multipolar moment and its far-field scattering contribution. In the following, we perform the multipole far-field scattering of resonance modes. From Fig. 3(a), we can see that at the resonance, the ED and TD dominate the scattering power and the scattered powers of ED and TD cross each other at 0.842 THz. The radiation of other multipoles is relatively small. To see this clearly, Fig. 3(c) and (e) shows the multipole decompositions of the scattered fields for individual cut-wire and two SRRs with gaps towards cut-wire, respectively. The predictable TD radiation has been predominant for cut-wire structure. For two SRRs structure, ED dominates the scattered powers as frequency is lower than 0.768 THz frequencies, and TD dominates between 0.768 and 1.4 THz. So the far-field scattering energy of coupled resonance mode is mainly contributed by the coupling of the ED and TD.

2.2. *The pattern of a cut-wire located between the SRRs with gaps inverse towards wire (pattern II)*

Secondly, we investigate the pattern with the gaps of two SRRs inverse toward cut-wire. The geometrical parameters are plotted in Fig. 4 (a) and the process of the optimization introducing the parameters *Ro/Ri/d/g/w/L* was provided in Supporting Information Section 1. As the polarization orientation of the excitation probe is taken along the *y*-direction, a clear split is recorded in the transmission response as illustrated in Fig. 4(b), dual resonances are found at 0.727 THz (f_1) and 0.905 THz (f_2). The surface currents are also obtained at f_1 and f_2 (Fig. 4 (c)). For this configuration, the central cut-wire acts as a 'bright'

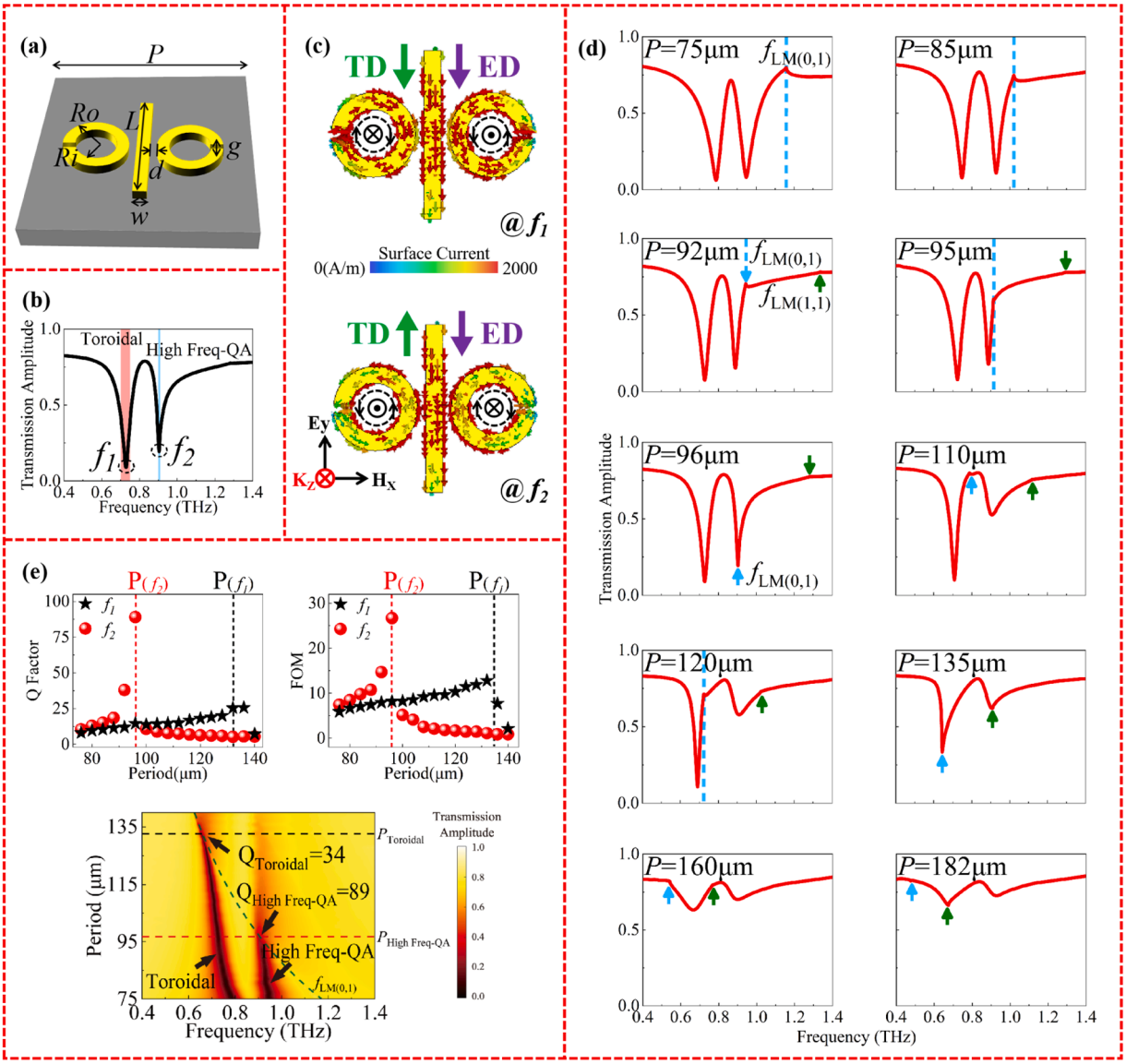

Fig. 4. (a) Unit cell of the metasurface, whose structural parameters are $P = 96$ μm, $L = 60$ μm, $w = 6$ μm, $g = 3$ μm, $d = 3$ μm. (b) The transmission amplitude of the metasurface. The resonances at f_1 and f_2 are marked as toroidal (red) and high frequency QA (blue), respectively. (c) The surface current distributions at f_1 and f_2 from front view. (d) Transmission spectra modulated by the lattice mode via manipulating P from 75 μm to 182 μm. Cyan dotted lines/arrows indicate the lattice mode (0, 1), while green arrows indicate the lattice mode (1, 1). Critical periods P are 96 and 135 μm, where the (0, 1) lattice mode matches high frequency QA and toroidal modes, respectively. (e) Top: *Q*-factor and *FOM* of the toroidal (black) and high frequency QA (red) at different lattice periods. Bottom: 2D transmission amplitude map as a function of period and frequency of the incident THz wave. The high frequency QA resonance is narrowest when it coincides with the lattice mode $f_{LM(0,1)}$ for critical periods $P_{high\ frequency\ QA} = 96$ μm and $P_{toroidal} = 135$ μm (dashed lines).

resonator and is able to directly couple to the incident THz field, while the side SRRs are 'dark' under the current probe beam polarization configuration. For the low frequency resonance, the induced current on the left SRR is in the clockwise direction while that on the right SRR is in the anti-clockwise direction, and the current on the central cut-wire runs from top to bottom as shown in Fig. 4(c). ED and TD are in phase and constructively interfere, which does not corresponds to the anapole mode. This mode can be referred to as toroidal or 'antibonding' mode. In the case of high frequency resonance, ED and TD are out of phase and QA mode is excited, which is consistent with the first configuration. This mode can also be referred to as 'bonding' mode.

We also studied the interaction between the lattice mode and the high frequency QA mode. The simulated transmission spectra by varying P are shown in Fig. 4(d). For a period of $P = 75$ μm, the lattice mode (indicated by the cyan dotted line/arrow) occurs at 1.16 THz, which is higher than the QA resonance frequency. Resonant coupling between the lattice mode and the QA resonance can be observed as the lattice period is increased from 75 to 96 μm. We see a narrower QA resonance as the lattice mode (cyan dotted line) approaches the QA resonance with increasing lattice period. When the lattice resonance frequency matches the QA resonance at $P = 96$ μm, the QA resonance has the narrowest linewidth. Further increasing the lattice period ($P > 96$ μm) may decrease the strength of the QA resonance and broaden its linewidth. Similar coupling behavior is observed for the low frequency toroidal resonance for periods from $P = 110$–182 μm. The top panels of Fig. 4(e) show the Q-factor and FOM by tuning the lattice mode frequency with increase of P. As P is From 75–96 μm, the Q-factor of QA increases gradually and the optimal P is 96 μm for the maximum Q-factor of 89. The highest Q-factor of 34.6 for low frequency toroidal mode locates at $P = 135$ μm. A similar trend is seen for the FOM, which also increases with increasing lattice period as the lattice mode frequency approaches the QA resonance, reaching a maximum value of $FOM = 26.7$ at $P = 96$ μm and a maximum of $FOM = 13.7$ for the toroidal mode at $P = 135$ μm. The bottom panel of Fig. 4(e) shows the 2D simulated transmission amplitude spectra map as a function of the lattice period. Since hybrid mode of LQA shows higher Q-factor and FOM than that of lattice enhanced toroidal, it is suitable for ultrasensitive THz immunosensor.

We calculated scattered powers for multipole moments to further analyze the role of TD and ED in the observed resonance, as shown in Fig. 5. It is clear that ED and TD show the two strongest scattered powers in the considered frequency range, meaning that the pattern in Fig. 5(b) is mainly excited by the electrical composition of the incident electromagnetic wave. Furthermore, the scattered powers of ED and TD cross at 0.710 and 0.905 THz, between which TD dominates the scattered powers. For toroidal mode around 0.727 THz, the TD emission is about 6.7 and 225.3 times than those of the ED and EQ, respectively. For QA mode at 0.905 THz, TD is the same as ED, and EQ and MQ are only one thousands of that of ED, leading to nonradiative anapole resonance. The corresponding phases of ED and TD were also calculated in supplementary materials of Section 2. We can see that at 0.727 THz (f_1) the phase difference is zero, indicating that ED and TD are in phase and this mode is not the anapole mode. While, at 0.905 THz, the phase difference is π, indicating destructive interference between ED and TD occurs and this mode is QA mode. The results agree with Fig. 4(c).

The electric-field, magnetic field, and electric energy density for pattern I at the resonance (0.842 THz) are shown in Fig. 6(a) (b) and (c), respectively. The electric field and electric energy density in the x-y plane demonstrated the localized electric field intensity at the capacitive gaps and both end of cut-wire. Besides, the vectorial profile for the x-z plane magnetic-field (H-field) intensity provides verification for the creation of closed-loop magnetic field around the cut-wire (Fig. 6(b)). For pattern II, the electric field and electric energy density in the x-y plane are much stronger than those of pattern I, especially by comparing the energy around SRRs gap in Fig. 6(c) and (f). The magnetic-field intensity in pattern II (Fig. 6(e)) shows much enhancement than that in pattern I (Fig. 6(b)), indicating stronger ED and TD moments. The sensitivities of high frequency QA and single QA modes are 126 GHz/RIU and 49 GHz/RIU, respectively (see detailed discussing in supplementary materials of Section 3). The sensitivity of high frequency QA is much higher than that of single QA, resulting in better immunesensor performance [51,52].

3. THz immunosensor based on LQA hybrid mode

3.1. Sample preparation and testing method

S protein and Anti-S were purchased from Lezee Biotechnology Co., LTD; AuNPs, Bovine Albumin (BSA), Phosphate buffered saline (PBS, pH = 6.47) were purchased from Sigma-Aldrich; Aβ40, Aβ42, CEA were provided by Shanghai Oriental Hospital. The immunosensor is characterized using a THz-TDS system which is produced by Advantest Test Company (China) (TAS 7500). The effective spectral range is 0.5–4 THz, with a spectral resolution of approximately 1.9 GHz. To mitigate interference from water vapor, all tests are conducted under conditions of room temperature at 23 ℃ and relative humidity below 4%. Repetitive testing is performed on all samples to ensure the robustness of the results.

3.2. Detection of S protein and Anti-S

Here, the designed high Q-factor LQA metasurface is used to achieve THz immunesensor. Firstly, the biosensor is utilized without modified Anti-S on surface. Instead, 10 μl S protein/Anti-S solution (the solvent is PBS) is dropped directly onto the metasurface and left to incubate for 1 h at 25 °C. The metasensor is placed in a 25 °C environment to be dried by air. The analyte on the metasurface is the mixture of PBS solute and S protein with different concentrations. The concentration of S protein increases from 10 pg/ml to 125 pg/ml and the Anti-S concentration increases from 10 pg/ml to 200 pg/ml. As shown in Fig. 7(b) and (c) show the transmission spectra responses and frequency shift of the high Q-factor LQA metasurface coated on S protein and Anti-S, respectively.

The frequency shift with respect to different concentrations of S

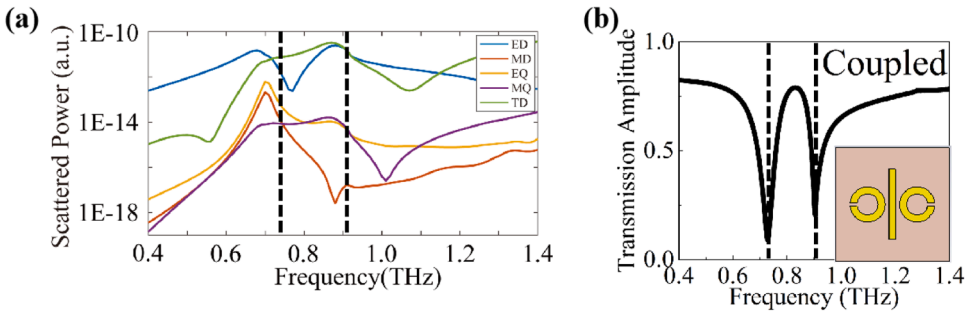

Fig. 5. (a) Multipole far-field scattering of coupled structure (b) The transmission spectrum of the coupled structure; the parameters are the same as those in Fig. 4(a).

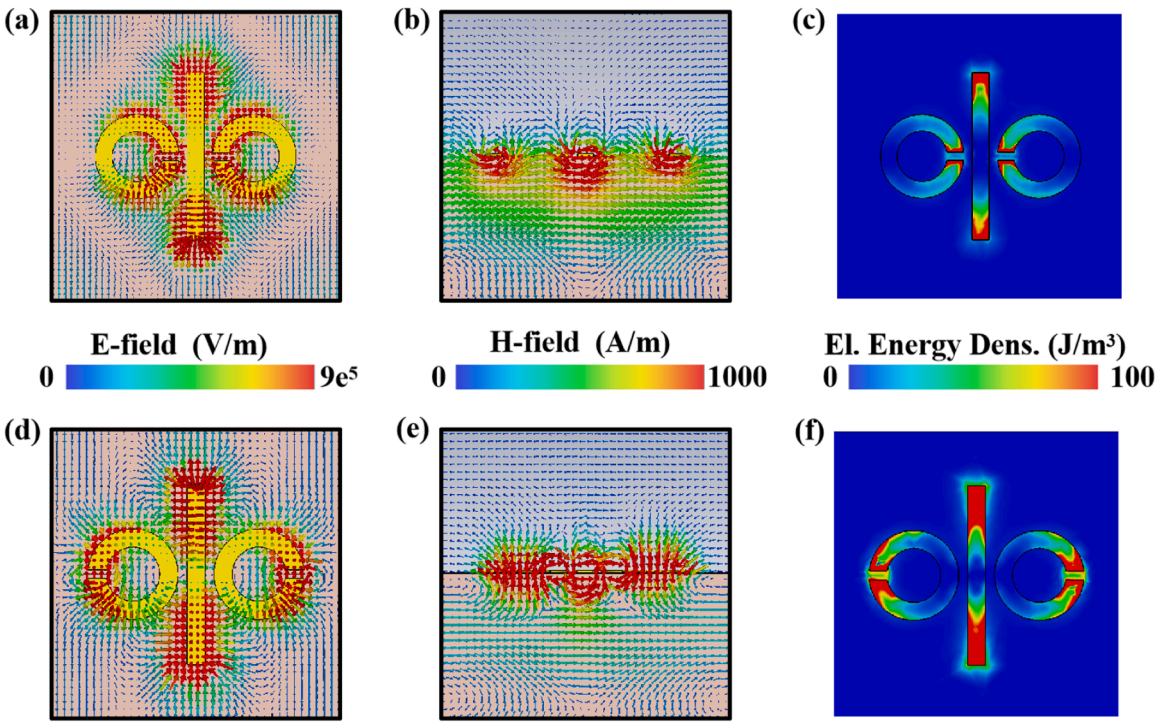

Fig. 6. Electric field in the *x-y* plane at (a) 0.842 THz in pattern I (d) 0.905 THz in pattern II; magnetic field in the *x-z* plane at (b) 0.842 THz in pattern I (e) 0.905 THz in pattern II; and electric energy density at (c) 0.842 THz in pattern I (f) 0.905 THz in pattern II.

protein and Anti-S solutions are shown in Fig. 7(b) and (c), respectively. With the increase of the concentration of S protein and Anti-S solution, the resonance frequencies both produce a red shift. The right panels of Fig. 7(b) and (c) shows linear correlations between the frequency shift and the concentration of S protein and Anti-S solution, respectively. For S protein, the linear equation was obtained by fitting the function: $Y = 0.132X + 9.849$, where X is the concentration of S protein. The *LoD* of S protein was 10 pg/ml. As the minimum frequency domain resolution ~1.9 GHz, the theoretical *LoD* can be achieved $1.9/0.132 = 14.4$ pg/ml.

3.3. Modification of immunosensor surface

To further improve the sensitivity and *LoD*, the immunosensor is proposed, whose surface was modified with AuNPs and Anti-S. AuNPs have the characteristics of good biocompatibility and easy to modification. So it is used to enhance the connect antibodies and effectively maintain activity [53–56]. The modification requires several steps including chemical modification of antibody and AuNPs prior to conjugation depending on the selected coupling chemistry. The sulfhydryl group is very attractive for conjugation of Anti-S to AuNPs since it forms a strong Au-S bond. The following steps were designed to modify Anti-S on the immunosensor surface (see Fig. 8(a)). The immunosensor is washed with an ultrasonic cleaner for 1 min. Then, 3-mercaptopropionic acid (MPA) with concentration of 5 mmol/L is dropped to the surface of sensor and incubated at 25 °C for 20 min. 10 μl of AuNPs is added on the surface of the immunosensor, and incubated at 4 °C for 70 min [53]. Transmission electron microscopy images at different magnifications were used to characterize the morphology of the prepared AuNPs (Fig. 8(b)). The AuNPs were robustly covalently conjugated by forming Au-S bonds with MPA. After that, the unbound solution on the surface is washed by using 99% absolute ethanol. The Anti-S solution is added on the surface of the immunosensor and incubated at 25 °C for 30 min. In order to lock the site of the AuNPs that are not bound to the Anti-S, 1 wt% bovine serum albumin (BSA) solution is added to the surface of the immunosensor, and then the immunosensor is placed at 25 °C for 30 min. The S protein solution is added to the surface and then incubated at 25 °C for 30 min.

3.4. Sensor specific detection

Three different concentrations of Anti-S solutions were configured after AuNPs was added to the surface and dried. For the first group of experiments, concentration of Anti-S solution was selected as 10 pg/ml, corresponding to the situation of low antibody concentration; Concentration of Anti-S solution was 50 pg/ml in the second group of experiments; For the third group of experiments, concentration of Anti-S solution is 200 pg/ml, corresponding to the high concentration of antibodies. In the experiment, Anti-S solution was dropped onto the surface and then incubated for 1 h for achieving immunosensor. Then different concentrations of S protein solution were dropped onto the immunosensor surface which has been modified by Anti-S to observe responses of THz transmission spectra.

The top left panel of Fig. 8(c) shows transmission spectra of the first experiment group. With the increase of the concentration of S protein, the QA resonance frequencies show red shift. The frequency shift becomes smaller with the increase of concentration of S protein. Since concentration of Anti-S solution was as low as 10 pg/ml, as the concentration of S protein was larger than that of the Anti-S, small amount of antigen binded with antibody and most of the S protein was not involved in the reaction. The frequency shift due to increased unbinded S proteins was less than binded immune complexes. We also used the Hill model to fit the relationship between the frequency shift and the concentration of S protein solution [52,57]:

$$\Delta f = \Delta f_{\max} \cdot \frac{[S]^m}{[K_D]^m + [S]^m} \tag{2}$$

where the maximum peak frequency shift. $\Delta f_{\max}$ is the saturation value, [S] is the concentration solution of S protein, m is the Hill coefficient, and K_D is the dissociation constant. The fitted curve is shown in the top right panel of Fig. 8(c). The Hill coefficient m can be obtained as 1.4, and the dissociation constant K_D is 13 pg/ml and Δf_{max} is 14.7 GHz.

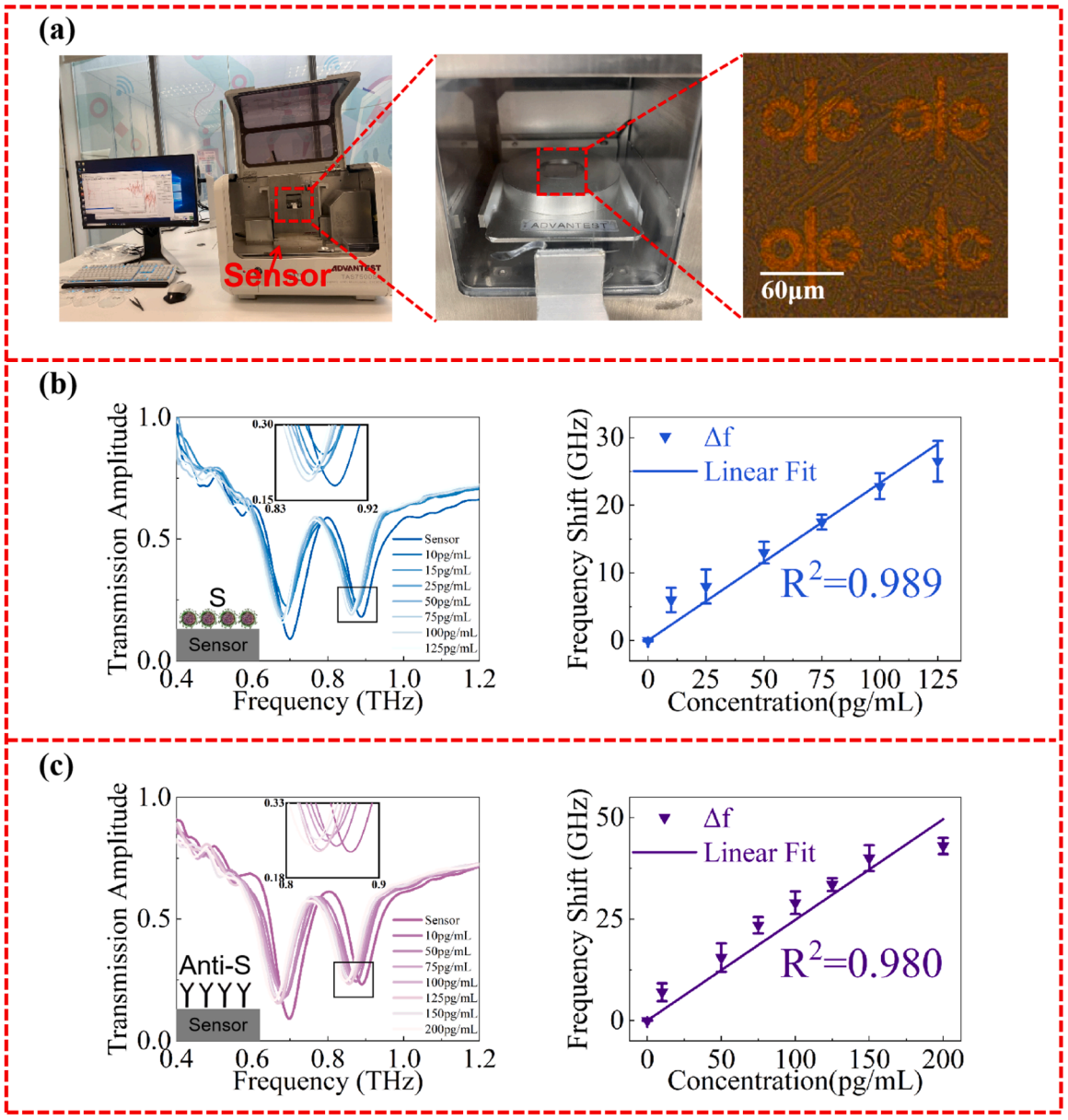

Fig. 7. (a) Left and Middle: Equipment diagram; Right: The optical microscopy images of dried analyte. (b) Left: Transmission spectra responses of LQA metasurface for different concentrations of S protein; Right: The frequency shift induced by S protein concentration. (c) Left: Transmission spectra responses of LQA metasurface for different concentrations of Anti-S; Right: The frequency shift induced by Anti-S concentration.

The middle left panel of Fig. 8(c) shows transmission spectra of the second experiment group with 50 pg/ml Anti-S solution. Frequency shift with respect to concentration of S protein solution was illustrated in the middle right panel of Fig. 8(c). At this time, the antigen and antibody were fully binded on the immunosensor surface, resulting in the gentle slope change of the curve in the middle right panel of Fig. 8(c). The fitting parameters in Eq. (1) are Hill coefficient $m = 1.7$, the dissociation constant $K_D = 19.6$ pg/ml and $\Delta f_{max} = 40.2$ GHz, respectively.

The bottom left panel of Fig. 8(c) plots transmission spectra by using 200 pg/ml Anti-S solution. The bottom right panel of Fig. 8(c) shows the variation of resonance frequency versus different S protein concentration. It can be seen that the frequency shift decreased slowly as the concentration of S protein increased, which was similar to the first experiment group, but their biological mechanisms were different. Since the concentration of antigen was always less than the concentration of Anti-S, there were three situations in the third experiment group: (1) the binding between antibody and antigen; (2) the binding between antibodies; (3) reaction between antibody and binded immune complexes. The products from the latter two situations could prevent and slow down/stop the progression of the binding [45,46]. So, excess antibodies can block the antigen-antibody binding. The Hill coefficient m, dissociation constant K_D, and Δf_{max}, are 0.6, 29.8 pg/ml and 47.3 GHz, respectively, which are fitted from the curve in the bottom right panel of Fig. 8(c).

The Hill model shows that the dissociation constant K_D is closely related to the concentration of S proteins. The *LoD* C_{lim} of S protein can be calculated using the following formula [55]:

$$C_{\text{lim}} = K_D \times \frac{S_f}{\Delta f_{\text{max}} - S_f} \tag{3}$$

Where, S_f is the minimum spectral resolution, which is 1.9 GHz in our experiment. The relationship between C_{lim} and antibody concentration is shown in Fig. 8(d). With the increase of antibody concentration, the theoretical *LoD* obtained from Eq. (3) first decreased and then increased.

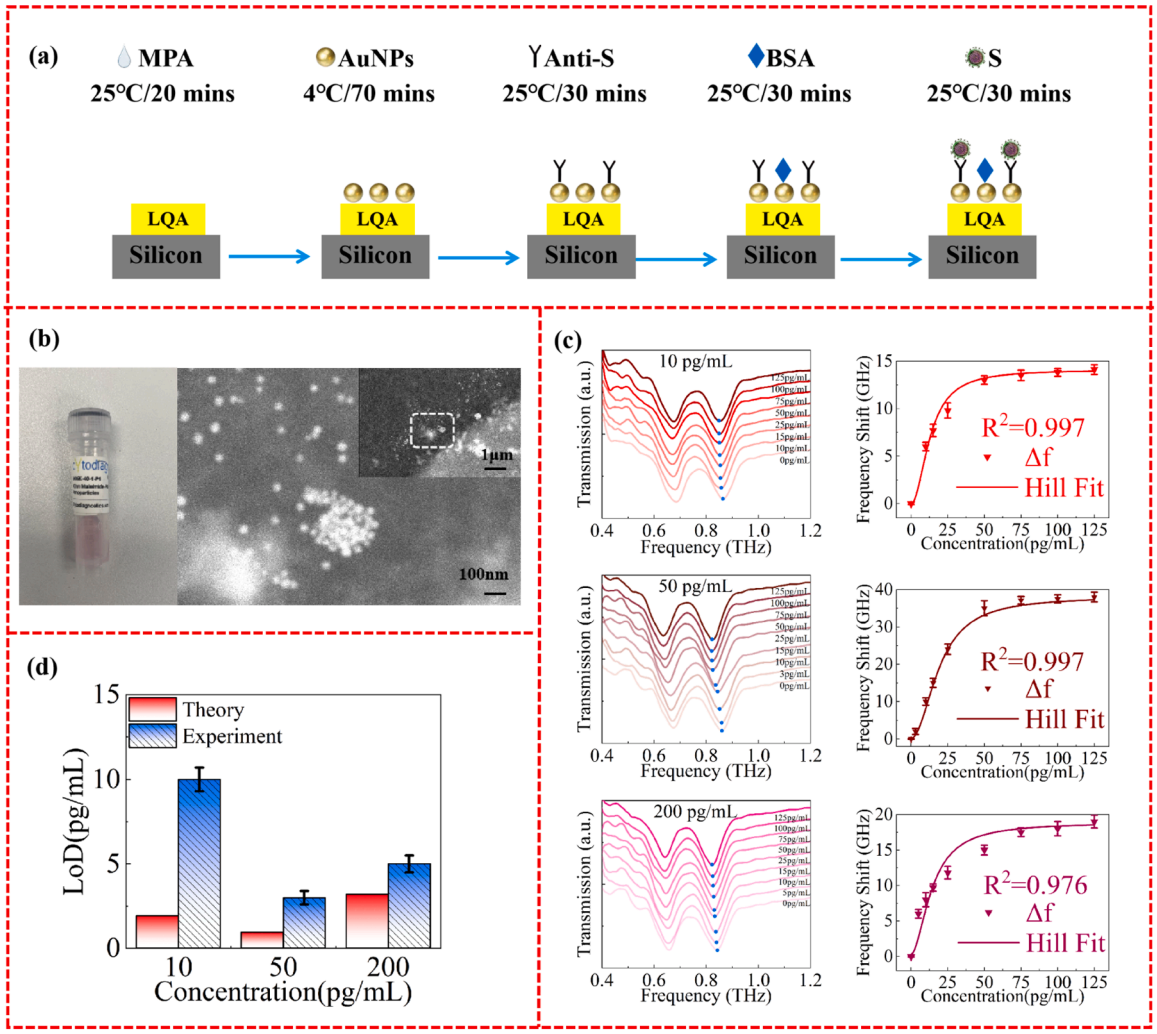

Fig. 8. (a) Schematic of the sensor surface modification. (b) Transmission electron microscopy (TEM) images of the AuNPs at different magnifications. The immunosensor surface was modified with Anti-S at different concentrations: (c) Top: transmission spectra with antibody concentration of 10 pg/ml and corresponding frequency shift versus S proteins concentrations; Middle: with antibody concentration of 50 pg/ml; Bottom: with antibody concentration of 200 pg/ml. (d) Experimental and theoretical *LoD* of antigen concentration. Red: theoretical calculations, blue: experimental results.

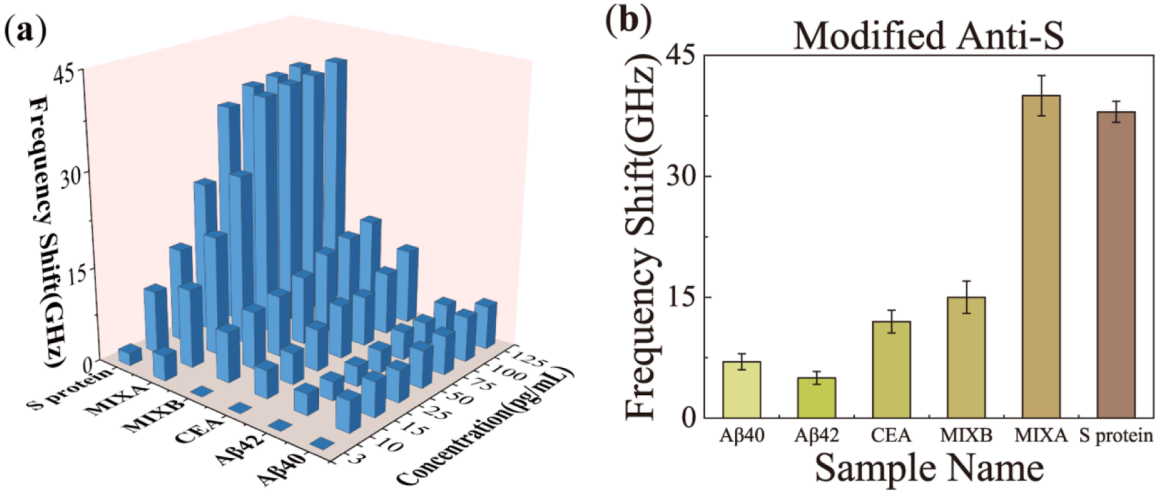

Fig. 9. (a) Specificity of the THz LQA-immunosensor for detecting target S protein. (b) The THz LQA-immunosensor detects the specificity of different samples at an antibody concentration of 50 pg/ml.

This is because when the antibody concentration is 50 pg/ml, the antigen is fully binded with antibody and the whole binding process is adequate. When the Anti-S concentration achieved 50 pg/ml, the *LoD* was as low as 0.95 pg/ml, which was significantly better than the result in Section 3.1. So 50 pg/ml concentration of Anti-S was used for optimal frequency shift.

3.5. Specific analysis

To verify the immunosensor has specific recognition of S protein, a controlled experiment was designed and conducted with the experiment result shown in Fig. 9. MIXA is a mixed solution of Aβ40, Aβ42, CEA and S protein, and MIXB is a mixed solution of Aβ40, Aβ42 and CEA. The difference between the two is that MIXA contains the target marker S protein. As can be seen from the figure, the frequency shift generated by MIXA and S protein samples is significantly higher than that of other samples, that is, the frequency shift of the resonance peak in the presence of S protein is significantly higher than that in the absence of S protein. Therefore, it can be considered that the sensor modified with Anti-S has a specific recognition capability for S protein. Through this experiment, we proved that antibody modification of the sensor surface improves the sensor's capability to detect the target antigen. The results showed that after modified antibody sensors that the sensor has the ability of specificity of detection.

4. Discussion and conclusion

Finally, we summarized and listed important results of this work and that of the recently reported immunosensors (Table 1). Biosensors are sensitive to biological substances and convert their concentration into an electrical signal for detection. While immunosensors are an important branch of biosensors that use highly specific binding between antibodies and antigens to recognize chemicals such as proteins. Our observations indicate that the LQA resonance exhibits superior sensing capabilities. This can be attributed to the phenomenon that QA modes are inducible within configurations that decreases radiation loss by suppressing both electric and toroidal dipole moments. The novel LQA metasurface demonstrates enhanced *Q*-factor stemed from the lattice mode's capability to confine electromagnetic fields and engage with the QA response of the metamaterial unit cell. This interaction augments the confinement of resonant fields and further mitigates radiative losses. Consequently, this minimized radiative loss endows the LQA structure with a higher *Q*-factor and *FOM*.

In summary, we performed novel THz LQA-immunosensor for specific detection of S protein. As the ED and TD possess different magnitudes and opposite phases, they partly cancel out mutual scattering in the far-field region and the QA mode is excited. We also discovered the coupling of QA modes and lattice structures for the first time. Coupling the lattice mode with the QA resonance of the metamaterial unit can diminish resonant radiation losses, thereby increasing its *Q*-factor. Through comparative experiments, we found that the experimental *LoD*s obtained by the immunosensor modified with AuNPs and antibodies were significantly lower than those by the unmodified metasensor. This shows the great advantage of THz LQA immunosensors for pg/ml level S protein detection. In addition, the *LoD*s are significantly influenced by concentration of antibody, resulting in biological mechanism of protein binding. Moreover, the LQA immunosensor has the ability of specificity of S protein detection. Hence, the proposed THz LQA-immunosensor demonstrates the remarkable promise for applications in virus and protein detection. Furthermore, it holds significant potential for the creation of a dependable virus screening chip, which would possess label-free attributes, exceptional sensitivity, noninvasive characteristics, and rapid detection capabilities.

Table 1
Comparison of current THz metamaterial strategies for protein detection.

Metasensor	Excited mode	Sample	*Q*-factor	*LoD*	References
biosensor	LC	HER2	9.71	0.1 ng/ml	[58]
immunosensor	LC	CA125 CA199	/	0.01 U/ml	[28]
biosensor	LC	S protein	/	5 ng	[59]
immunosensor	toroidal	CEA	15.04	0.17 ng	[60]
biosensor	toroidal	Zika-virus protein	18	24 pg/ml	[29]
biosensor	toroidal	S protein	14.5	4.2 fM	[54]
immunosensor	LQA	S protein	89	3 pg/ml	This work

Funding

This project was supported by the National Natural Science Foundation of China (Nos. 61988102, and 62275157), the Shuguang Program supported by the Shanghai Education Development Foundation and the Shanghai Municipal Education Commission, China (No. 18SG44), the 111 Project (D18014).

CRediT authorship contribution statement

Chengcheng Luo: Writing – review & editing, Writing – original draft, Visualization, Software, Resources, Methodology, Investigation, Formal analysis, Data curation. **Ranjan Singh:** Writing – review & editing, Visualization, Supervision, Resources, Project administration, Investigation, Data curation, Conceptualization. **Lin Chen:** Writing – review & editing, Writing – original draft, Visualization, Validation, Supervision, Software, Resources, Project administration, Methodology, Investigation, Funding acquisition, Formal analysis, Data curation, Conceptualization. **Zhiyuan Fan:** Writing – review & editing, Software, Investigation, Data curation. **Thomas Tan CaiWei:** Writing – review & editing, Supervision, Software, Investigation, Data curation, Conceptualization. **Yiming Zhu:** Writing – review & editing, Investigation, Funding acquisition. **Songlin Zhuang:** Writing – review & editing, Funding acquisition.

Declaration of Competing Interest

The authors declare the following financial interests/personal relationships which may be considered as potential competing interests: Lin Chen reports was provided by Basic Science Center Project of the National Natural Science Foundation of China. Lin Chen reports was provided by National Natural Science Foundation of China. Lin Chen reports was provided by Shanghai Shuguang Program. Lin Chen reports was provided by 111 Project.

Data availability

Data will be made available on request.

Acknowledgments

We thank Xujun Yuan from Shanghai Cohere Electronic Technology Company and Xi Zhang from Shanghai Municipal Center For Disease Control & Prevention for fully discussion about S protein.

Appendix A. Supporting information

Supplementary data associated with this article can be found in the online version at doi:10.1016/j.snb.2024.135628.

References

[1] Ruth M. Woodward, et al., Terahertz pulse imaging in reflection geometry of human skin cancer and skin tissue, Phys. Med. Biol. 47 (21) (2002) 3853–3863.
[2] B.M. Fischer, M. Walther, A.P.U. Jepsen, Far-infrared vibrational modes of DNA components studied by terahertz time-domain spectroscopy, Phys. Med. Biol. 47 (21) (2002) 3807–3814.
[3] L. Chen, et al., Terahertz time-domain spectroscopy and micro-cavity components for probing samples: a review, Front. Inf. Technol. Electron. Eng. 20 (5) (2019) 591–607.
[4] X. Zang, et al., Metasurfaces for manipulating terahertz waves, Light.: Adv. Manuf. 2 (2) (2021) 148–172.
[5] Q.P. Zeng, et al., Aptamer HB5 modified terahertz metasurface biosensor used for specific detection of HER2, Sens. Actuators B-Chem. 355 (2022) 131337.
[6] I. Al-Naib, Biomedical sensing with conductively coupled terahertz metamaterial resonators, IEEE J. Sel. Top. Quantum Electron. 23 (4) (2017) 1–5.
[7] L. Chen, et al., Mode splitting transmission effect of surface wave excitation through a metal hole array, Light.: Sci. Appl. 2 (3) (2013) p. e60-e60.
[8] C. Weisenstein, et al., Ultrasensitive THz biosensor for PCR-free cDNA detection based on frequency selective surfaces, Biomed. Opt. Express 11 (1) (2020) 448–460.
[9] L. Rong, et al., Terahertz in-line digital holography of human hepatocellular carcinoma tissue, Sci. Rep. 5 (1) (2015) 8445.
[10] M. Beruete, I. Jáuregui-López, Terahertz sensing based on metasurfaces, Adv. Opt. Mater. 8 (3) (2019) 1900721.
[11] Fabio Alves, et al., Narrowband terahertz emitters using metamaterial films, Opt. Express 20 (19) (2012) 21025–21032.
[12] D.R. Smith, J.B. Pendry, M.C.K. Wiltshire, Metamaterials and negative refractive index, Science 305 (5685) (2004).
[13] Y. Zhu, et al., Metasurfaces designed by a bidirectional deep neural network and iterative algorithm for generating quantitative field distributions, Light.: Adv. Manuf. 4 (1) (2023) 9.
[14] J.B. Pendry, et al., Extremely low frequency plasmons in metallic mesostructures, Phys. Rev. Lett. 76 (25) (1996) 119701.
[15] J.B. Pendry, et al., Magnetism from conductors and enhanced nonlinear phenomena, IEEE Trans. Microw. Theory Tech. 47 (11) (1999) 2075–2084.
[16] D.R. Smith, et al., Composite medium with simultaneously negative permeability and permittivity, Phys. Rev. Lett. 84 (18) (2000) 4184–4187.
[17] H. Tao, et al., Performance enhancement of terahertz metamaterials on ultrathin substrates for sensing applications, Appl. Phys. Lett. 97 (26) (2010) 261909.
[18] H. Tao, et al., Metamaterials on paper as a sensing platform, Adv. Mater. 23 (28) (2011) 3197–3201.
[19] L. Chen, et al., Defect-induced fano resonances in corrugated plasmonic metamaterials, Adv. Opt. Mater. 5 (8) (2017) 1600960.
[20] J. Lyu, et al., Frequency selective fingerprint sensor: the Terahertz unity platform for broadband chiral enantiomers multiplexed signals and narrowband molecular AIT enhancement, PhotoniX 4 (1) (2023) 28.
[21] J. Lyu, et al., Review on the terahertz metasensor: from featureless refractive index sensing to molecular identification, Photonics Res. 12 (2) (2024) 194–217.
[22] A. Ahmadivand, et al., Terahertz plasmonics: the rise of toroidal metadevices towards immunobiosensings, Mater. Today 32 (2020) 108–130.
[23] Tan, Plum, Singh, Surface lattice resonances in THz metamaterials, Photonics 6 (3) (2019).
[24] M. Gupta, R. Singh, Terahertz sensing with optimized Q/Veff metasurface cavities, Adv. Opt. Mater. 8 (16) (2020) 1902025.
[25] J. Xu, et al., Terahertz microfluidic sensing with dual-torus toroidal metasurfaces, Adv. Opt. Mater. 9 (15) (2021) 2100024.
[26] T.C. Tan, et al., Active control of nanodielectric-induced THz Quasi-BIC in flexible metasurfaces: a platform for modulation and sensing, Adv. Mater. 33 (27) (2021) 2100836.
[27] Z. Li, X.-W. Luo, Q. Gu, Topological on-chip lasers, APL Photonics 8 (7) (2023).
[28] S. Lin, et al., Detection of cancer biomarkers CA125 and CA199 via terahertz metasurface immunosensor, Talanta 248 (2022), p. 123628-123628.
[29] A. Ahmadivand, et al., Rapid detection of infectious envelope proteins by magnetoplasmonic toroidal metasensors, ACS Sens. 2 (9) (2017) 1359–1368.
[30] Y. Yang, S.I. Bozhevolnyi, Nonradiating anapole states in nanophotonics: from fundamentals to applications, Nanotechnology 30 (20) (2019), p. 204001-204001.
[31] A.A. Basharin, et al., Extremely high Q-factor metamaterials due to anapole excitation, Phys. Rev. B 95 (3) (2017) 035104.
[32] M. Gupta, R. Singh, Toroidal versus Fano Resonances in High Q planar THz Metamaterials, Adv. Opt. Mater. 4 (12) (2016) 2119–2125.
[33] S. Han, et al., Toroidal and magnetic Fano resonances in planar THz metamaterials, J. Appl. Phys. 122 (11) (2017), p. 113105-113105.
[34] X. Liu, et al., Tunable terahertz metamaterials based on anapole excitation with graphene for reconfigurable sensors, ACS Appl. Nano Mater. 3 (3) (2020) 2129.
[35] M.V. Cojocari, K.I. Schegoleva, A.A. Basharin, Blueshift and phase tunability in planar THz metamaterials: the role of losses and toroidal dipole contribution, Opt. Lett. 42 (9) (2017) 1700–1703.
[36] R. Wang, L. Dal Negro, Engineering non-radiative anapole modes for broadband absorption enhancement of light, Opt. Express 24 (17) (2016) 19048–19062.
[37] S.D. Liu, et al., High Q-factor with the excitation of anapole modes in dielectric split nanodisk arrays, Opt. Express 25 (19) (2017) 22375–22387.
[38] A.K. Ospanova, I.V. Stenishchev, A.A. Basharin, Anapole mode sustaining silicon metamaterials in visible spectral range, Laser Photonics Rev. 12 (7) (2018) 1800005.
[39] J.F. Algorri, et al., Ultrahigh-quality factor resonant dielectric metasurfaces based on hollow nanocuboids, Opt. Express 27 (5) (2019) 6320–6330.
[40] K.V. Baryshnikova, et al., Optical anapoles: concepts and applications, Adv. Opt. Mater. 7 (14) (2019) 1801350.
[41] P. Klarskov, et al., Amplification of resonant field enhancement by plasmonic lattice coupling in metallic slit arrays, Sci. Rep. 6 (1) (2016) 37738.
[42] A. Halpin, et al., Terahertz diffraction enhanced transparency probed in the near field, Phys. Rev. B 96 (8) (2017) 085110.
[43] Andreas Bitzer, et al., Lattice modes mediate radiative coupling in metamaterial arrays, Opt. Express 17 (24) (2009) 22108–22113.
[44] Ningning Xu, Ranjan Singh, aW. Zhang, High-Q lattice mode matched structural resonances in terahertz metasurfaces, Appl. Phys. Lett. 109 (2) (2016) 021108.
[45] Thomas C.W. Tan, Eric Plum, aR. Singh, Lattice-enhanced fano resonances from bound states in the continuum metasurfaces, Adv. Opt. Mater. 8 (6) (2020) 1901572.
[46] T.C. Tan, et al., Lattice induced strong coupling and line narrowing of split resonances in metamaterials, Appl. Phys. Lett. 112 (20) (2018).
[47] C. Huang, et al., Clinical features of patients infected with 2019 novel coronavirus in Wuhan, China, Lancet 395 (10223) (2020) 497–506.
[48] S. Kasetsirikul, et al., Detection of the SARS-CoV-2 humanized antibody with paper-based ELISA, Analyst 145 (23) (2020) 7680–7686.
[49] Q. Bayin, et al., Anti-SARS-CoV-2 IgG and IgM detection with a GMR based LFIA system, Talanta 227 (2021), p. 122207-122207.
[50] L. Cong, et al., Fano resonances in terahertz metasurfaces: a figure of merit optimization, Adv. Opt. Mater. 3 (11) (2015) 1537–1543.
[51] R. Singh, et al., Ultrasensitive terahertz sensing with high-Q Fano resonances in metasurfaces, Appl. Phys. Lett. 105 (17) (2014) 171101.
[52] Y.K. Srivastava, L. Cong, R. Singh, Dual-surface flexible THz Fano metasensor, Appl. Phys. Lett. 111 (20) (2017), p. 201101-201101.
[53] S. Engel, E.C. Fritz, B.J. Ravoo, New trends in the functionalization of metallic gold: from organosulfur ligands to N-heterocyclic carbenes, Chem. Soc. Rev. 46 (8) (2017) 2057–2075.
[54] A. Ahmadivand, et al., Functionalized terahertz plasmonic metasensors: Femtomolar-level detection of SARS-CoV-2 spike proteins, Biosens. Bioelectron. 177 (2021) 112971.
[55] L. Zhang, et al., Antibody-gold nanoparticle bioconjugates for biosensors: synthesis, characterization and selected applications, Biosens. Bioelectron. 165 (2020), p. 112370-112370.
[56] L. Cui, et al., Construction of a dye-sensitized and gold plasmon-enhanced cathodic photoelectrochemical biosensor for methyltransferase activity assay, Anal. Chem. 93 (29) (2021).
[57] W. Fu, et al., Qualitative and quantitative recognition of volatile organic compounds in their liquid phase based on terahertz microfluidic EIT meta-sensors, IEEE Sens. J. 23 (12) (2023) 7962–7971.
[58] Q.P. Zeng, et al., Aptamer HB5 modified terahertz metasurface biosensor used for specific detection of HER2, Sens. Actuators B: Chem. 355 (2022).
[59] Q. Niu, R. Zhang, Y. Yang, High sensitivity and label-free detection of the SARS-CoV-2 S1 protein using a terahertz meta-biosensor, Front. Phys. 10 (2022).
[60] Q. Niu, et al., Sensitive and specific detection of carcinoembryonic antigens using toroidal metamaterial biosensors integrated with functionalized gold nanoparticles, Anal. Chem. 95 (2) (2023).

Chengcheng Luo received the M.S. degree in College of Science, University of Shanghai for Science and Technology in 2020. She is pursuing the PhD degree in optical engineering with University of Shanghai for Science and Technology, Shanghai, China. Her research interests is in terahertz metasensor, material, and immune motification.

Thomas Tan CaiWei received diploma in Aeronautical Engineering and certificate in Engineering from Singapore Polytechnic in 2010, Bachelor of Applied Science from Nanyang Technological University in 2016, and PhD of Physics from Nanyang Technological University in 2020. He is now Research Fellowship of Nanyang Technological University. His research interest is terahertz metamaterial and surface lattice management with bound states in the continuum, and 2D terahertz imaging platform for beam steering.

Zhiyuan Fan received his B.S. in Applied Physics and B.E. in Computer Engineering in 2005, M.S. in Optics from Shanghai Jiaotong University in 2008, and PhD in Condensed Matter Physics from the Ohio University, Ohio, USA in 2014. He pursued research in metamaterials at the University of Texas at Austin from 2014 to 2016 and was an academic researcher from Cornell University from 2016 to 2021. He is now a professor of optical engineering at the University of Shanghai for Science and Technology. His research interest covers the circular dichroism in plasmonic metamaterials, tunable metamaterials and optoelectronics for THz biosensing.

Lin Chen received the B.S. and M.S. degrees in electrical engineering from Southeast University, Jiangsu, China, in 2002 and 2005, respectively, and the Ph.D. degree in optics from Shanghai Jiao Tong University, Shanghai, China, in 2008. From 2007–2008, he was with Avanex Corporation as Senior Engineer. From 2012–2013, he was a Visiting Scholar with the State Key Laboratory of Millimeter Waves, Southeast University. From 2015–2016, He was a Visiting Researcher with Ultrafast THz Optoelectronic Laboratory, Oklahoma State University, Stillwater, OK, USA. He was designated Shanghai "Dawn scholar", "Chengguang scholar", "Top-Notch Young Talents", "Rising-Star", "Pujiang talent" and other talent titles. He was also award Publons Peer Review Award (2018 and 2019) and Best Researcher Award on Atomic, Molecular and Optical Physics (2024). As the first person in charge, he has undertaken a number of national level projects, including the

national key R&D plan "major scientific instrument and equipment development" (chief scientist), two national major instrument projects (project), National Natural Foundation of China (general & Youth) and several projects in Shanghai. At present, He has published more than 70 peer reviewed papers with more than 2000 citations and H-index 26 (including 4 Highly Cited Paper) in Science Citation Indexed journal such as Light: Science & Applications, etc. He has also applied for more than 40 invention patents, 21 authorized and 1 US patent. He is currently the Editorial Board Member of Frontiers in Physics, Guest Editor and Corresponding Expert of Frontiers of Information Technology & Electronic Engineering.

Ranjan Singh is an Associate Professor at NTU Singapore. He received a Ph.D. in Photonics from Oklahoma State Univ. (2009). He then joined Los Alamos National Laboratory. In 2013, he founded TeraX Labs at the Centre for Disruptive Photonic Technologies (CDPT), NTU. He is an OSA Fellow for pioneering contributions to terahertz science and technology. His research interest includes terahertz for 6 G communications, metasurfaces, and light-induced high-Tc superconductivity. He has raised US$ 12 M in competitive research grants. Since 2020, he has been listed as the top 1% highly cited researcher.

Yiming Zhu graduated from the University of Tokyo with a Ph.D. degree. He is a "Youth Science and technology innovation leader" and "Young Yangtze Professor" in the University of Shanghai for Science and Technology, and currently serves as a vice director of the Shanghai Key Lab of Modern Optical System. He is also the "The national key talent project", "Outstanding Youth Foundation", and "special State Council allowance" winner. His research focuses on terahertz technologies and applications, including terahertz devices, terahertz spectroscopy, imaging systems, terahertz bio-applications, etc.

Songlin Zhuang graduated from Physics Department of Fudan University in 1962. From 1962–1979, he worked in Shanghai Institute of Optical Instruments. In 1979, he went to Michigan State University (USA) for visiting research, and in 1982 he obtained his doctorate in the Department of Electronic Engineering of Pennsylvania State University (USA). In 1983, he returned to Shanghai Institute of Optical Instruments as director and senior engineer. From 1988–1992, he served as director and researcher of Shanghai Institute of Laser Technology. Since 1995, he has been the president of School of Optical-Electronic and Computer Engineering, University of Shanghai for Science and Technology. He has won many ministerial level science and technology progress awards and many honorary awards. He is the first researcher to carry out optical system CAD in China. He has made a comprehensive and systematic research on incoherent optical information processing and rainbow holography, and is known as "one of the main contributors of modern white light information processing".